Supplementary Information

Superresolution imaging reveals nanometer- and micrometer-scale spatial distributions of T-cell receptors in lymph nodes

Ying S. Hu[a,b], Hu Cang[b,1] and Björn F. Lillemeier[a,b,1]

Affiliation:

[a] Nomis Center for Immunobiology and Microbial Pathogenesis, Salk Institute for Biological Studies, La Jolla, CA 92037, USA

[b] Waitt Advanced Biophotonics Center, Salk Institute for Biological Studies, La Jolla, CA 92037, USA

[1] To whom correspondence should be addressed. Emails: blillemeier@salk.edu and hucang@salk.edu

Keywords:

T-cell receptor, T-cell activation, protein cluster, superresolution, plasma membrane

Materials and Methods

Mice, antibodies and peptides

The animal protocol was approved by the Salk Institutional Animal Care and Use Committee (protocol #13-00006). Mouse experimental procedures were performed according to the guidelines of the Public Health Service Office of Laboratory Animal Care and the Salk Institute for Biological Studies. Armenian hamster monoclonal H57 anti-murine TCR β-chain (Bio-X-Cell), clone N418 anti-murine CD11c (eBioscience), and B220 (eBiosceince) were used to label T cells dendritic cells, and B cells in 5c.c7 TCR transgenic mice. Mouse monoclonal Clone 1F8-1E4 anti-fluorescein-isothiocyanate (FITC; Thermo Scientific) was used to label MCC (MCC^{FITC}; Eton Bioscience). The MCC peptide (amino acids 88-103 of moth cytochrome C) was synthesized and HPLC purified at the Salk Institute Peptide Synthesis Core.

Fluorophore conjugation of antibodies

To label H57 and 1F8-1E4 antibodies, Alexa Fluor 647 (AF647) NHS ester (Life Technologies) was dissolved in dimethylformamide (DMF) at 2mg/ml. Antibodies (2mg/ml) were mixed with 5-fold molar excess of AF647 in 0.1M bicarbonate pH 8.3 and 150mM NaCl at room temperature for 2h. The reaction was stopped with 50mM glycine. Excess fluorophore was removed using a 40kD cut-off desalting column (Thermo Scientific). Antibodies were stored at 4ºC in phosphate buffered saline (PBS). The labeling ratios for both were determined to be ~2.5 fluorophores per antibody.

Lymph node preparation

For analyses of activated T cells, 5c.c7 mice were intraperitoneal (i.p.) injected with an emulsion of alum adjuvant [5% $KAl(SO_4)_2$ in phosphate buffered saline pH7.2] and 100µg MCC peptide. Mesenteric lymph nodes were prepared immediately after euthanasia using CO_2 followed by cervical dislocation. Lymph nodes were cut into 2-3mm pieces, fixed in 4% (w/v) paraformaldehyde for 24h, and cryo-protected overnight at 4ºC in 30% (w/v) sucrose solution. Cryo-protected tissues were transferred to optimum cutting temperature (OCT) compound and sectioned at thicknesses of 10µm and 50µm on a Leica cryostat. Tissue sections were affixed to 0.1% w/v poly-L-lysine (Sigma) coated 22mm glass coverslips (Fisher Scientific), and air-dried overnight at room temperature before immunofluorescence staining.

Immunofluorescence staining

a. Tissue staining: Tissue sections were rinsed in PBS and blocked in 5% (w/v) BSA, 0.1% (v/v) FCS, and 0.3% Triton for 2h at room temperature, and stained overnight with 2μg/ml H57^{AF647} at 4ºC. Stained samples were rinsed five times (10m each) in PBS before imaging.

b. Cell staining: Naïve cells were isolated from mesenteric lymph nodes and immediately fixed with 2% PFA. Immunofluorescent staining using H57^{AF647} was performed without permeabilizaiton for 2h at room temperature in the blocking buffer (5% (w/v) BSA, 0.1% (v/v) FCS) at the antibody concentration of 2μg/ml. Cells were washed and post-fixed with 4% PFA and 0.1% glutaraldehyde for 15m, and subsequently quenched with 0.1% sodium borohydride for 10m. Stained cells were spun on glass surfaces of 8-well chamber slides (Lab-Tek II) at 1000 rpm for 5m.

c. Single antibody coating: H57 antibodies were incubated with poly-l-lysine coated glass surfaces at a final concentration of 2μg/ml for 1h at room temperature. H57^{AF647} conjugates were titrated by unlabeled H57 antibodies at ratios from 10:1 to 100:1. Surfaces were washed and coated with streptavidin-tagged gold nanoshells (nanoComposix, Lot # JMW1901) prior to imaging.

Fluorescence super-resolution imaging

a. Light sheet system

Single-molecule super-resolution imaging was performed using a previously reported prism-coupled light-sheet system (1). The custom set-up was adapted to a Zeiss Examiner.D1 upright microscope. The collimated excitation laser (Coherent Cube, 642nm, 100mW) passed through a cylindrical lens (f = 500 mm, Thorlabs), after which the tangential plane (horizontal to the optical table) of the laser was focused onto the back aperture of the illumination objective (50x/0.55 Mitutoyo M Plan Apo, WD = 200mm), while the sagittal plane remained collimated (*i.e.* the laser cross-section appeared as a vertical line at the back aperture). The illumination objective was horizontally placed before a glass prism with a slanted top surface of ~20 degrees. The sagittal plane, which correlates with the thickness of the light sheet, was focused onto the top surface of the glass prism. The tangential plane, which correlates with the width of the light sheet, was collimated. To visualize the light sheet, 35-mm glass-bottom-dish containing dark red fluorescent bead solution (1×10^6 /ml, LifeTech) was placed onto a custom-made sample holder. The emission filter set included a single-band band-pass filter (692/40nm, Semrock), a long-pass filter (532nm, Semrock), and a 633nm single-notch filter (Semrock). An Andor iXon DU-897E EMCCD camera with a pixel size of 16×16μm was used for imaging. A 2.5x magnifier was placed in the filter cube, rendering an effective pixel size of 102nm in the imaging plane. The imaging arm on the upright microscope was placed on a base plate and translated until the field of view from the imaging objective (Plan-Apochromat, 63x/1.0W, water immersion; Zeiss) overlapped with the light sheet illumination volume.

The profile of the light sheet was monitored by using 40-nm red (660/680 ex/em) fluorescent microsphere solution (LifeTech F8789) with a titration of $1{:}10^4$ from the stock solution. After removing the cylindrical lens, the thickness of the light sheet was measured from the full-width half-maximum of the intensity profile from averaging 1000 frames. At the thinnest portion of the light sheet, the FWHM was less than 2µm (Fig. S1B). To determine the thickness of the light sheet in tissue, 1000 image frames was collected inside a 50-um-thick tissue section with low laser intensity to reduce bleaching. Averaged tissue fluorescence was obtained by translating H57-stained tissue along the light sheet illumination (Fig. S1D). Compared to the profile in solution, the thinnest portion was approximately 40% thicker at 2.7µm. The increased thickness is likely due to tissue scattering.

b. Light sheet *d*STORM Imaging

Continuous 642-nm light sheet excitation intensity was ~11 kW/cm^2 in the imaging plane. The excitation light sheet quickly switched off AF647 dyes in this region. A low-power 405-nm light laser (Coherent) with varying durations from 1ms to 0.5s was used for activation. For *d*STORM imaging, an aliquot of 200µl of the imaging buffer [50mM Tris pH8.0, 10mM NaCl, 10% glucose (w/v), 1mg/ml glucose oxidase (Sigma) and 40µg/ml catalase (Sigma), and 143 mM β-mercaptoethanol (Sigma)] was added to the space between the objective lens and the tissue. Typically 60,000 frames were collected with an integration time of 15ms. Drift correction was performed by cross correlating 2D histograms binned from single molecule localizations every 2000 frames.

Of note, drift correction using cross-correlation of event-based reconstructions has been previously implemented for single-molecule super-resolution imaging (2-4). In our correction method, image frames were divided into equal time intervals. In each interval, single molecule localizations were binned into 50×50nm pixels to form a reconstructed image. The X-Y drift was determined as the distance between the cross-correlation and auto-correlation peaks of reconstructed images from the current interval and the fist time interval. Sub-pixel cross-correlation using an up-sampling factor of 100 allowed us to achieve nanometer-scale precision. A MATLAB function *dftregistration* was adapted and used for drift calculation (5). To evaluate the effectiveness of sub-pixel cross-correlation, TIRF-*d*STORM imaging was performed on AF647-stained (Thermo Fisher A-21235) microtubules (Sigma T8328) in fixed MEF cells. The glass surface was coated with 150nm gold nanoshells as fiducials. Stage drifts were first characterized by a standard method using fiducial beads. Averaged results from fiducials were then compared with drifts correction using sub-pixel cross-correlation. Sub-pixel cross-correlation characterized stage drifts in a consistent manner with respect to traditional method using fiducials (Fig. S2). On one hand, a large number of frames per interval caused a slight "under-sampling" of the drift. On the other hand, a small number of frames per interval caused variations and noise drift correction. However, drift correction using sub-pixel cross-correlation was maintained within ~30nm range from the correction derived from fiducials. Moreover, the sub-pixel cross-correlation was shown effective in correcting "streaking" of microtubule fibers due to drift and was relatively insensitive to the number of frames binned in each interval (Fig. S3C).

To determine the localization precision of light sheet *d*STORM, photon count of each single molecule event was calculated based off a 7-by-7px area with the center position defined by the localization. The background level was calculated as the difference between a 8-by-8px area and the 7-by-7px area defined by the same center location, and averaged by the number of pixels in the outer peripheral (32 px). The intensity was obtained by integrating the A/D count of each pixel across the 7-by-7px area and subtracting the average background integrated over the same area (49 px). The original signal in electrons was calculated by multiplying the readout count with the iXon DU-897E CCD sensitivity of 10.57 electrons per A/D count at a system readout rate of 5MHz, 14-bit, and a pre-amp setting of 5, and dividing the number of electrons by the EM gain of 300. Photon conversion was done by dividing the original signal in electrons by the quantum efficiency of the camera of approximately 91.25% at 700-nm collection wavelength. The photon count histogram resembled a *log-normal* distribution (Fig. S4A). The mean photon count was 401 and the mean localization precision was 35nm (Fig. S4B). The photon count and localization precision are consistent with the literature (6-8). Single molecule events within 2.5 times the localization precision (35nm) from consecutive frames were grouped into a single localization event. The coordinate of the group event was determined by the weighed average of repeat events based on their intensity *(9, 10)*. Global estimate of the spatial resolution was estimated by Fourier Ring Correlation (FRC) analysis (11). In general, the lower bound of the spatial resolution was found to be approximately 50 nm through repeat analyses (Fig. S4C).

c. TIRF *d*STORM

TIRF was performed with the same excitation and activation lasers through a 100x/1.49 lens. The pixel size in the imaging plane was 160nm. Gold nanoshells with near infrared plasmonic resonance were placed on poly-l-lysine coated glass. IF stained cells were spun on glass surfaces and drift was corrected by using nanoshell fiducials. For *d*STORM imaging, an aliquot of 200µl of the imaging buffer containing 50mM Tris pH8.0, 10mM NaCl, 10% glucose (w/v), 0.8mg/ml glucose oxidase (Sigma) and 40µg/ml catalase (Sigma), and 100–200 mM cysteamine was used. 30,000 frames were collected at 30mS/frame for reconstruction. Repeat events from consecutive frames were grouped.

d. SIM imaging

Zeiss ELYRA PS.1 was used for SIM imaging. Tissue samples were embedded in Vectashield for index matching. A 100x/1.49 oil objective was used, and five rotations were acquired with the 0.51μm grid at 633nm excitation. Superresolution images were reconstructed with the following Method parameters: Processing: manual, Noise Filter: -1.0, SR Frequency Weighting: 1, Baseline Cut, Sectioning: 98/83/83, Output: SR-SIM, PSF: Theoretical.

*d*STORM and SIM of freshly isolated T cells from tissue

T cells from mice with or without antigen injection were isolated, washed once and immediately fixed in suspension at 2-4×10^6 T cells/ml to best preserve the membrane architecture. T cells were stained with H57^{AF647} in suspension without permeabilization to avoid labeling of intracellular TCRs, *i.e.* in microvesicles (12, 13). T cells were deposited on poly-L-lysine coated coverslips and analyzed by TIRF and SIM microscopy.

Computing nearest neighbor distance between protein islands

The distribution of TCR islands was quantified by the Euclidean distances from nearest neighbors. Local maxima on a pixel level in a 2D histogram showing protein islands were obtained by using a MATLAB function *pkfnd* developed by Eric R. Dufresne at Yale University. The threshold (*th*) and size (*sz*) parameters were interactively chosen so the majority of protein islands were identified as single peaks. A square sub-area corresponding to each peak in the raw image (with the center pixel coordinates defined by the output of *pkfnd* and width defined by *sz*).was extracted and the centroid positions were refined by non-linear fitting to the Gaussian form in both x and y positions using the MATLAB function *nlinfit.* With refined centroid positions, the Euclidean distances between nearest neighbors were obtained by the MATLAB function *knnsearch*.

Single antibody detection

Localizations from single antibody detections were first binned into a 2D probability histogram. The centroid positions of clusters were calculated by a Gaussian fit similar to the method used for single-molecule fitting. The boundaries of the clusters were defined as 200nm-by-200nm square boxes whose center positions were defined by the centroids of single molecule clusters. The number of events for each cluster was estimated within the square area. The same square area was used for estimating the number of clusters per protein island in Fig. 1.

References

1. Hu YS*, et al.* (2013) Light-sheet Bayesian microscopy enables deep-cell super-resolution imaging of heterochromatin in live human embryonic cells. *Opt Nanoscopy* 2(7).
2. Huang B, Wang W, Bates M, & Zhuang X (2008) Three-dimensional super-resolution imaging by stochastic optical reconstruction microscopy. *Science* 319(5864):810-813.
3. Geisler C*, et al.* (2012) Drift estimation for single marker switching based imaging schemes. *Opt Express* 20(7):7274-7289.
4. Mlodzianoski MJ*, et al.* (2011) Sample drift correction in 3D fluorescence photoactivation localization microscopy. *Opt Express* 19(16):15009-15019.
5. Guizar-Sicairos M, Thurman ST, & Fienup JR (2008) Efficient subpixel image registration algorithms. *Opt Lett* 33(2):156-158.
6. Cella Zanacchi F*, et al.* (2011) Live-cell 3D super-resolution imaging in thick biological samples. *Nat Methods* 8(12):1047-1049.
7. Ritter JG, Veith R, Veenendaal A, Siebrasse JP, & Kubitscheck U (2010) Light Sheet Microscopy for Single Molecule Tracking in Living Tissue. *Plos One* 5(7).
8. Gebhardt JC*, et al.* (2013) Single-molecule imaging of transcription factor binding to DNA in live mammalian cells. *Nat Methods*.
9. Veatch SL*, et al.* (2012) Correlation Functions Quantify Super-Resolution Images and Estimate Apparent Clustering Due to Over-Counting. *Plos One* 7(2).
10. Sengupta P*, et al.* (2011) Probing protein heterogeneity in the plasma membrane using PALM and pair correlation analysis. *Nat Methods* 8(11):969-975.
11. Nieuwenhuizen RP*, et al.* (2013) Measuring image resolution in optical nanoscopy. *Nat Methods* 10(6):557-562.
12. Friedman RS, Beemiller P, Sorensen CM, Jacobelli J, & Krummel MF (2010) Real-time analysis of T cell receptors in naive cells in vitro and in vivo reveals flexibility in synapse and signaling dynamics. *J Exp Med* 207(12):2733-2749.
13. Choudhuri K*, et al.* (2014) Polarized release of T-cell-receptor-enriched microvesicles at the immunological synapse. *Nature* 507(7490):118-123

Supplementary Figures

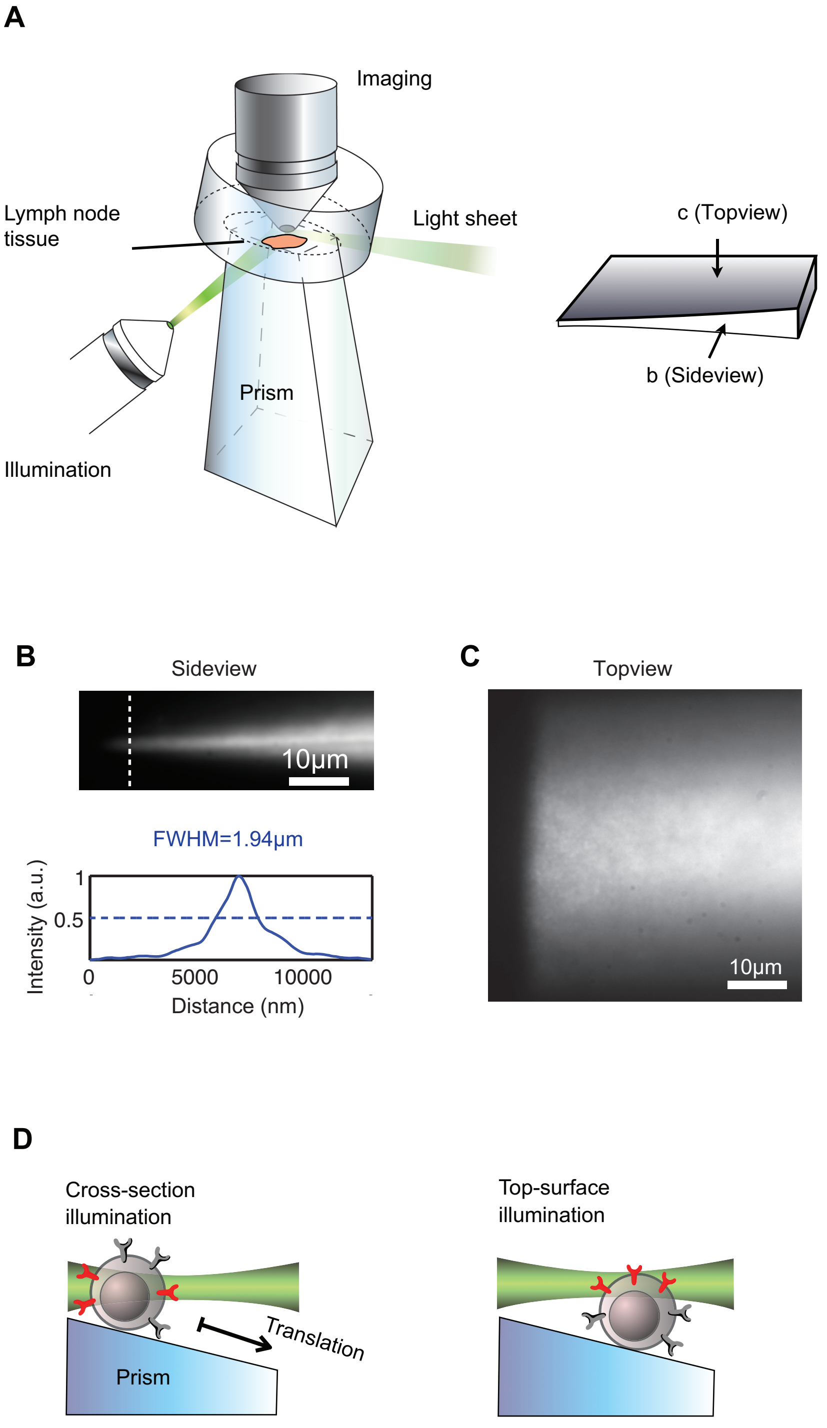

Fig. S1. Prism-coupled light-sheet *d*STORM. (**A**) Schematic of the prism-couped light sheet. (**B**) Sideview of the light sheet and its intensity profile in fluorescent bead solution. The thinnest portion of the light sheet is 1.94µm thick by full-width at half-maximum (FWHM). (**C**) Topview of the light sheet profile. (**D**) Translation of the sample with respect to the light sheet to image the cross-section and top-surface of cells.

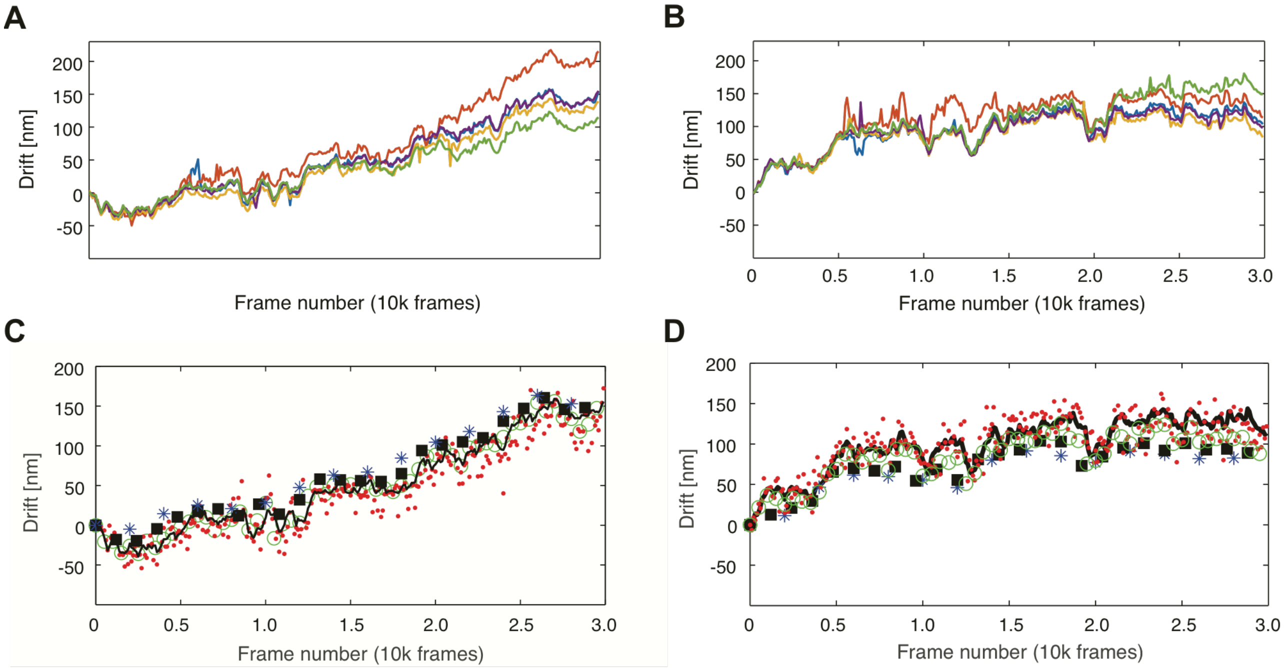

Fig. S2. Stage drift correction using fiducials and sub-pixel cross-correlation. (**a-b**) x and y drift characterized from five gold nanoshells. Solid line: average drift calculated from Gaussian fitting of 5 gold nanoshells fiducial particles on the glass surface. Dots: drift calculated from sub-pixel cross-correlation by binning every 100 frames (red dots), 500 frames (green circles), 1200 frames (solid rectangles), and 2000 frames (blue stars).

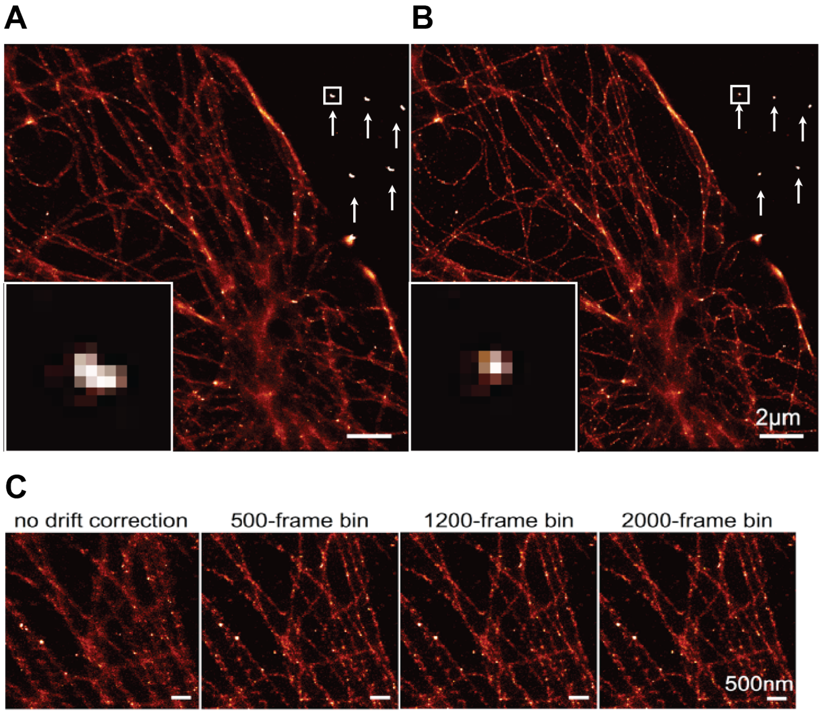

Fig. S3 Correcting drifts using sub-pixel cross-correlation in *d*STORM images of microtubule fibers. (**A**) Microtubule fibers imaged with the presence of stage drift. Arrows indicate positions of five fiducials. (**B**) *d*STORM image of (A) with drift correction using cross-correlation of every 500 frames. Inserts in (A) and (B) show image of single fiducial before and after drift correction using sub-pixel cross-correlation. (**C**) Higher magnification views of the drift correction by binning various numbers of frames in cross-correlation.

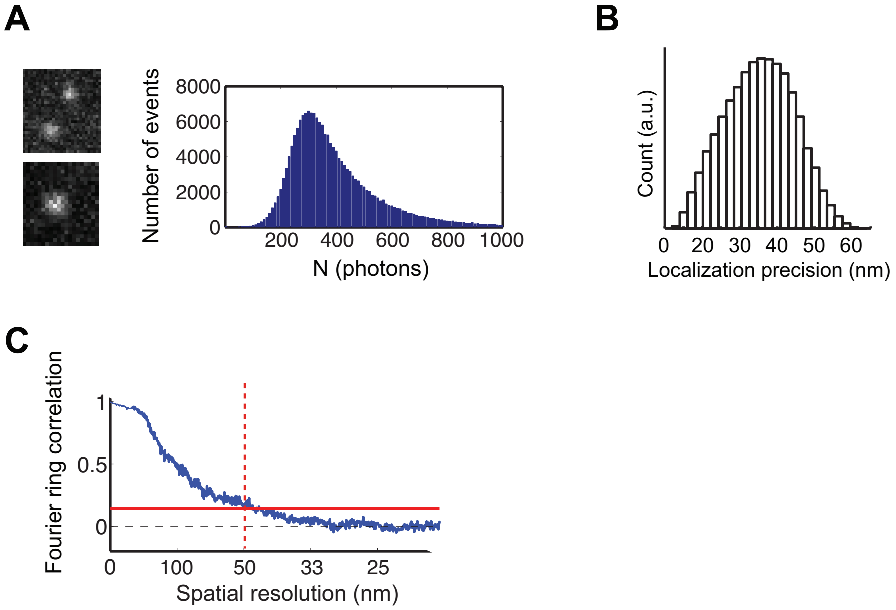

Fig. S4. (**A**) Representative single molecule events and estimation of the photon count, (**B**) localization precision, and (**C**) spatial resolution of the light-sheet *d*STORM system. The photon count follows a log-normal distribution. The mean localization precision was ~35nm. Fourier ring correlation analyses demonstrate the spatial resolution of ~50nm using the single-molecule data.

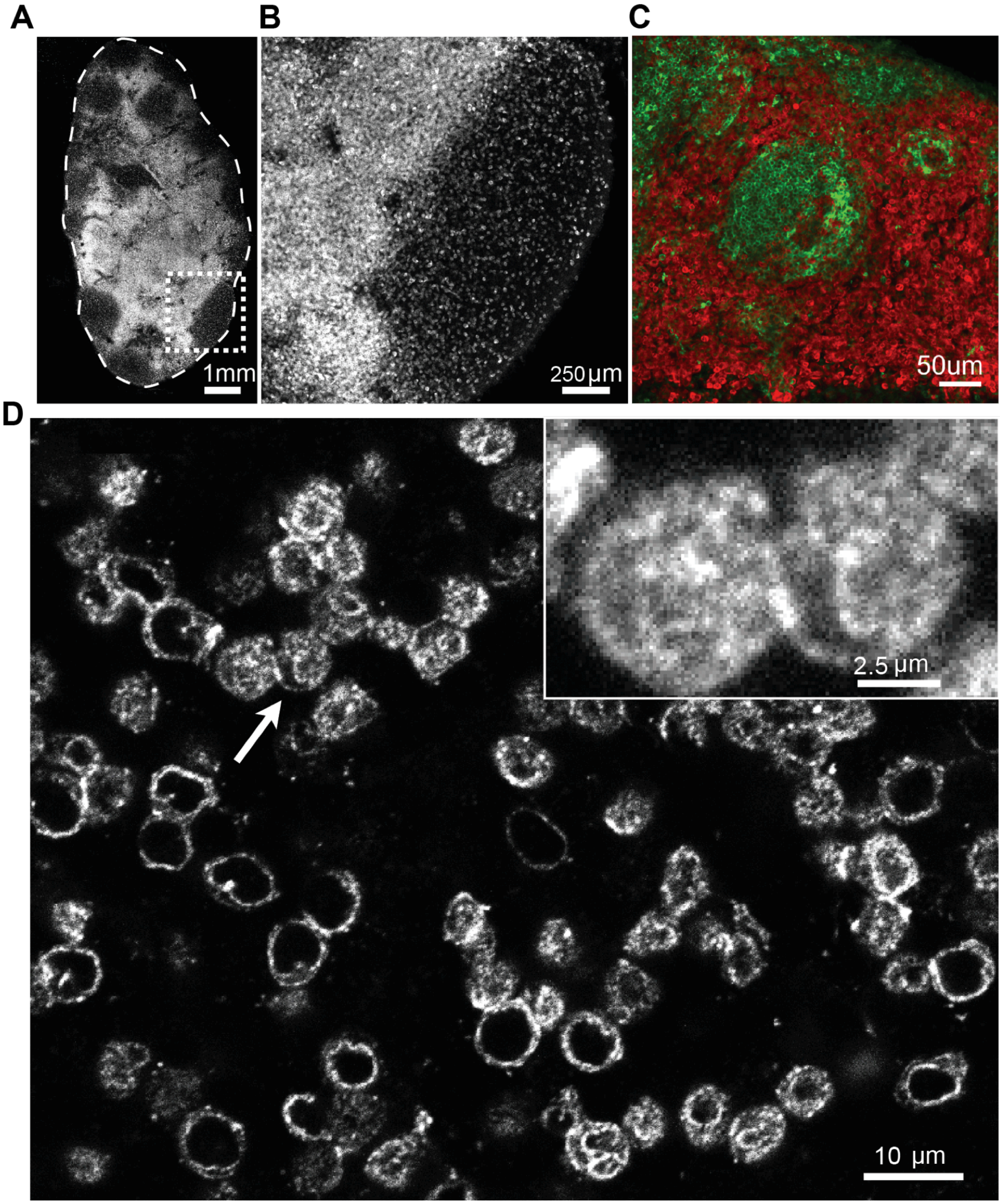

Fig. S5. Line scanning confocal images of TCRs in lymph node tissues. (**A**) A whole lymph node cross-section. (**B**) Boxed region in (a) showing the boundary between B cell follicles and T cell zones. (**C**) B and T cells in mesenteric lymph node tissue. B cells were stained with B220 (green) and T cells with H57 (red). (**D**) High-magnification view (100x) hinted that TCR were distributed in localized domains on the plasma membrane of naïve T cells in lymph node sections. Inset shows the region pointed by arrow.

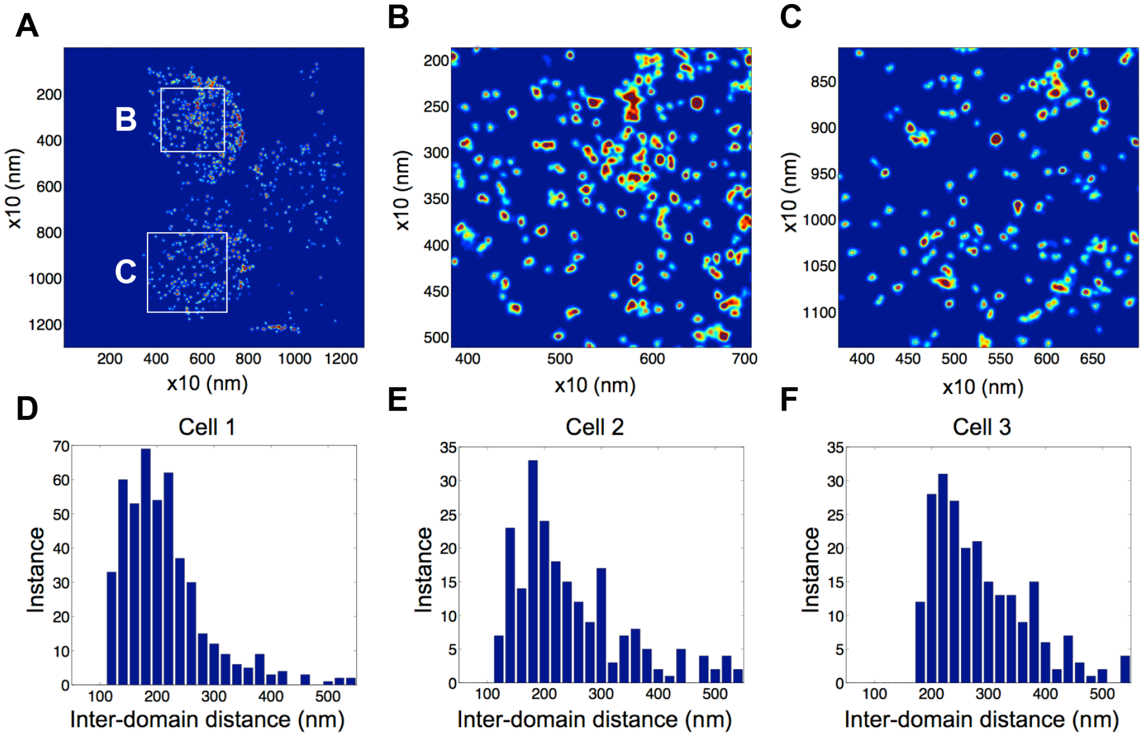

Fig. S6. Distributions of protein islands on naïve T cells and the inter-island distance distribution. (**A**) Light sheet dSTORM image of TCRs on naïve T cells in tissue. (**B**-**C**) High-magnification view of regions in (A). (**D**) Distribution of the nearest neighbor distances for protein islands in (A). (**E**-**F**) Distributions of the nearest neighbor distances for protein islands for two additional naïve T cells. The median separation was around or above 200nm.

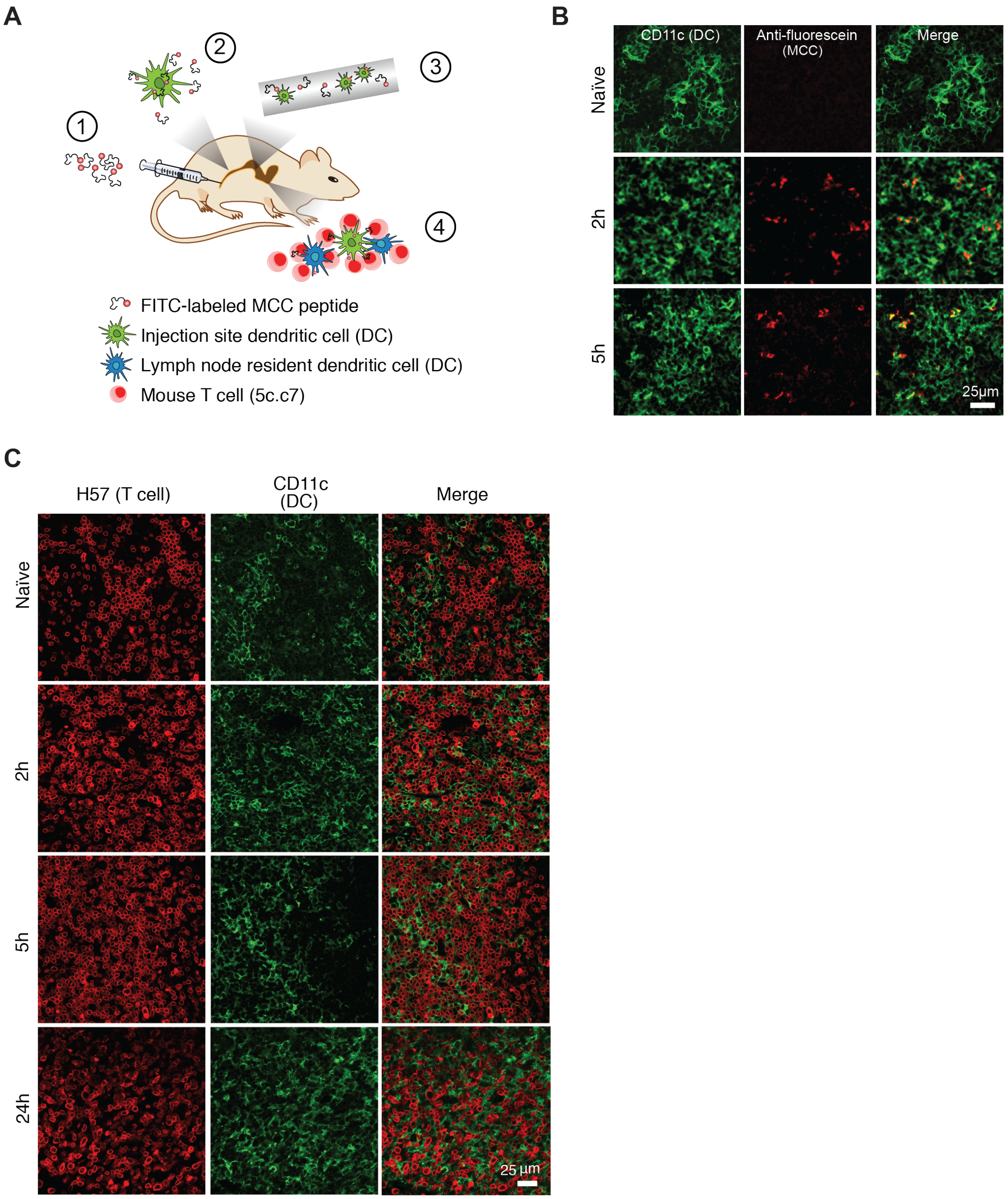

Fig. S7. *In vivo* T cell activation. (**A**) Schematic showing T cell activation *in vivo* using 5c.c7 TCR transgenic mice. Numbers indicate: 1): i.p. injection of FITC labeled MCC peptide; 2): uptake of the peptide by dendritic cells at the injection site; 3) MCC delivery to mesenteric lymph nodes by active DC transport and passive distribution *via* blood circulation; 4) peptide presentation by injection site DCs and resident DCs for activation of T cells in the lymph node. (**B**) Confocal images of dendritic cells and MCC peptides in lymph node tissues from mice without peptide injection (naïve), and two and five hours after peptide injection (activated). (**C**) Confocal images of T cells (red) and DCs (green) in mesenteric lymph node tissues from naïve, and 2, 5 and 24h post-injection of MCC into mice. T cells and DCs were co-stained by H57 and CD11c.

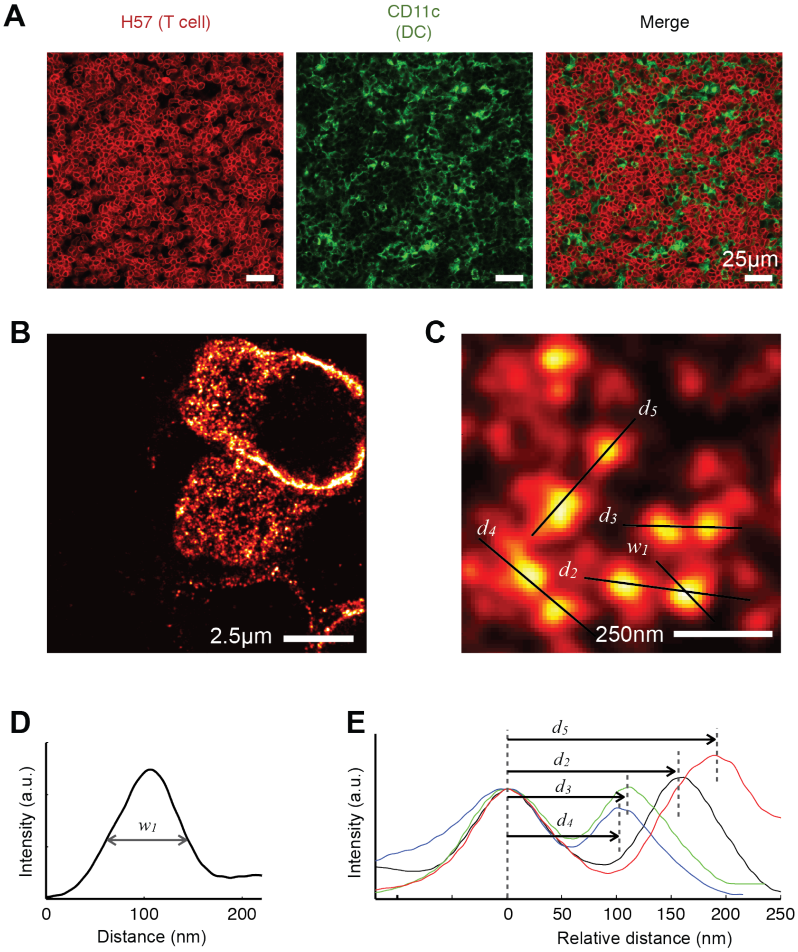

Fig. S8. TCR organization in T cells from mice 5h after injection of alum adjuvant without MCC (negative control). (**A**) Fluorescent images of T cells (stained by H57 ^{AF647}) and dendritic cells (DCs) (stained by CD11c ^{AF488}) in lymph node sections. (**B**) Light sheet *d*STORM image of TCRs on T cells from the control tissue shows distinct TCR islands and territories. (**C**) High-magnification view shows outlined TCR islands. (**D**) Line profiles showing the width and spacing between local density peaks: w_1 = 78nm, d_2 = 162nm; d_3 = 111nm; d_4 = 99; d_5 = 189nm.

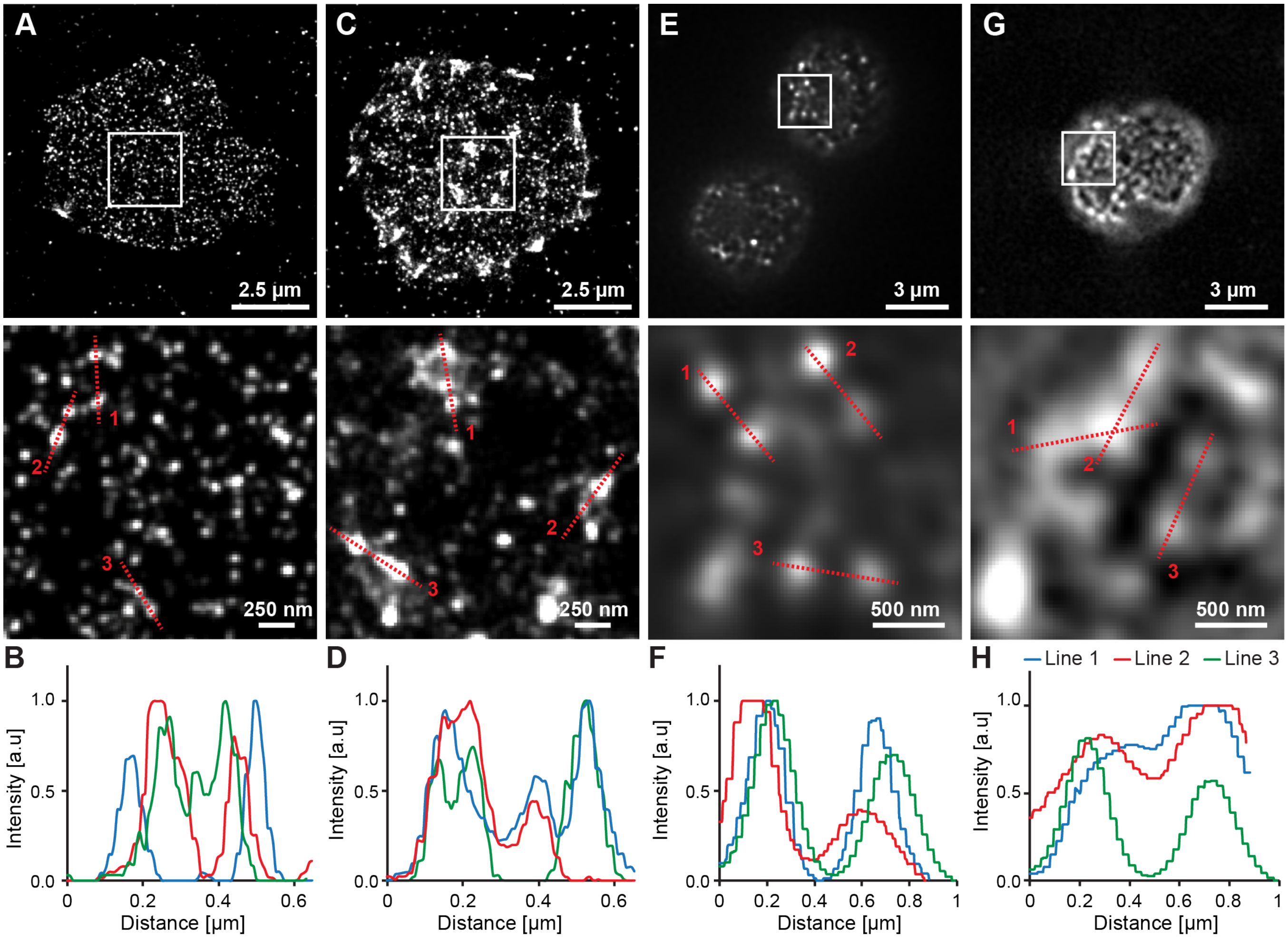

Fig. S9**.** *d*STORM and SIM images of fixed naïve and *in vivo* activated 5c.c7 cells freshly isolated from the mesenteric lymph nodes of mice. (**A**) *d*STORM image of TCRs on naïve cells. Lower image shows boxed region with higher magnification. (**B**) Line profiles of protein islands showing their separation by arrows. (**C**) *d*STORM image of an activated primary T cell. **(D)** Line profiles showing concatenation of protein islands by arrows and formation of microclusters. **(E)** SIM image of TCRs on naïve cells. **(F)** Line profiles of protein islands showing their separation. **(G)** SIM image of an activated primary T cell. **(H)** Line profiles showing concatenation of protein islands by arrows and formation of microclusters.

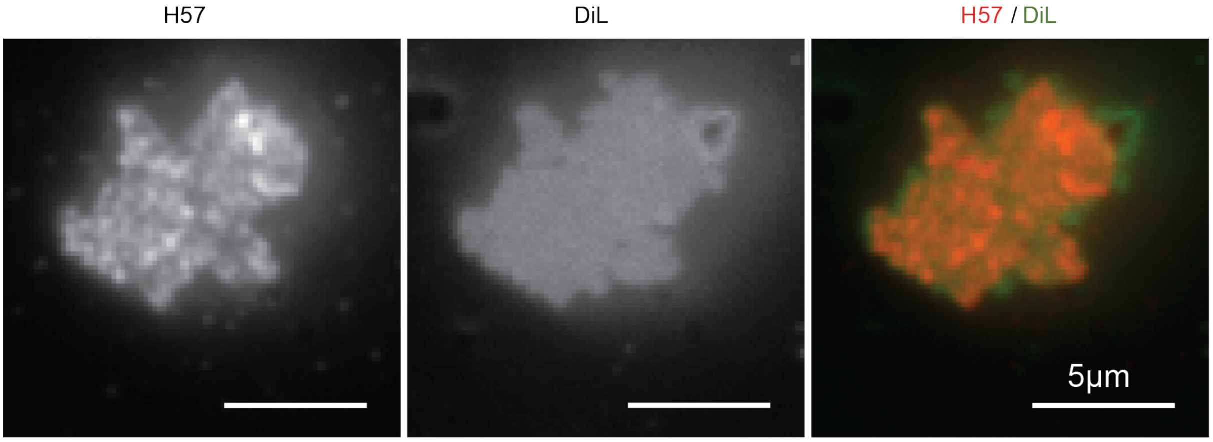

Fig. S10. TIRF imaging of DiL membrane stain showing that TCR clustering is not due to membrane ruffling.